Article

Effect of Annealing Environment on the Performance of Sol–Gel-Processed ZrO_2 RRAM

Seunghyun Ha [1], Hyunjae Lee [1], Won-Yong Lee [1], Bongho Jang [2], Hyuk-Jun Kwon [2], Kwangeun Kim [3] and Jaewon Jang [1,*]

[1] School of Electronics Engineering, Kyungpook National University, Daegu 41566, Korea
[2] Department of Information and Communication Engineering, Daegu Gyeongbuk Institute of Science and Technology (DGIST), Daegu 42988, Korea
[3] Department of Electronic and Electrical Convergence Engineering, Hongik University, Sejong 30016, Korea
* Correspondence: j1jang@knu.ac.kr

Received: 22 July 2019; Accepted: 26 August 2019; Published: 28 August 2019

Abstract: We investigate the annealing environment effect on ZrO_2-based resistive random-access memory (RRAM) devices. Fabricated devices exhibited conventional bipolar-switching memory properties. In particular, the vacuum-annealed ZrO_2 films exhibited larger crystallinity and grain size, denser film, and a relatively small quantity of oxygen vacancies compared with the films annealed in air and N_2. These led to a decrease in the leakage current and an increase in the resistance ratio of the high-resistance state (HRS)/low-resistance state (LRS) and successfully improved non-volatile memory properties, such as endurance and retention characteristics. The HRS and LRS values were found to last for 10^4 s without any significant degradation.

Keywords: sol–gel; ZrO_2; resistive random-access memory; annealing environment

1. Introduction

Memory cells are critical for electronic devices. Such devices include radio frequency identification devices, sensors, and next-generation display applications that are able to store signals. Due to the limitations of conventional memory devices, such as flash memory devices, resistive random-access memory (RRAM)—consisting of an active layer and two electrodes—is considered a promising approach that can be used to overcome such limitations. Advantages include low-power operation, a simple structure, and strong endurance and retention [1–3]. Moreover, promising candidate active materials for RRAMs include organic materials, metal oxides, and carbon-based materials [4–9]. Among these materials, metal oxides have the advantages of a large band-gap for fully transparent memory devices, chemical stability, and conventional CMOS-process-compatible properties. Recently, ZrO_2 dielectric materials have been employed to increase field-effect mobility by improving the interface quality [10–12]. To fabricate a single RRAM array, the selector (e.g., a thin-film transistor or diode) is required to solve the sneak path issue. A ZrO_2 layer can be used for both the gate insulator of the thin-film transistor and the main material for the RRAM, thus reducing the product cost. To reduce the production cost, recently, solution process techniques have been used to fabricate RRAM devices. Solution processing-based devices offer the advantages of low cost, simplicity, and compatibility with a spin-coating and printing system. For the realization of large and high-capacity memory arrays based on a single RRAM, a large high-resistance state (HRS)/low-resistance state (LRS) ratio is crucial [13,14]. In this study, the chemical and electrical properties of sol–gel-processed ZrO_2 resistive memory were analyzed to determine the impact of varying annealing environment conditions. Compared with a RRAM consisting of ZrO_2 layers annealed in air, the devices fabricated in this study, consisting of an annealed ZrO_2 layer in a vacuum, demonstrated an improved HRS/LRS ratio and endured over

~10^2 cycles with no significant degradation. Moreover, the device retained the HRS/LRS ratio for ~10^4 seconds.

2. Materials and Methods

To form an Ag/ZrO_2/ITO sandwich structure, the ZrO_2 layers were prepared using a sol–gel deposition method. A total of 0.001 mol of $Zr(C_5H_7O_2)_4$ was dissolved in 9.9 mL of ethanol to obtain a clear solution. Following this, 0.1 mL of ethanolamine was added as a stabilizer. The prepared solution was ultrasonicated for 1 hour to disperse the Zr precursor, thus obtaining a clear solution. Commercial indium tin oxide (ITO)-deposited glasses, used as the bottom electrode (BE), were ultrasonically cleaned with acetone and deionized water for 10 minutes, respectively. A UV/O3 cleaning process was then conducted for 10 minutes to remove surface contaminants. The prepared precursor solution was deposited on an ITO-glass through a spin-coating process (3000 rpm for 50 s) and immediately placed on a hot plate at 300 °C for 5 minutes in air to evaporate the solvent. Multiple processes were carried out to manipulate the insulator thickness (~50 nm). The soft baked samples were annealed in air, a vacuum, and flowing N_2 ambience at 500 °C for 2 hours, respectively. The pressure inside the tube furnace was maintained under 0.1 MPa in vacuum conditions, and N_2 gas was flowed into the tube at a rate of 3.0 L/min. Finally, 100 nm of Ag was deposited on a solid ZrO_2 layer using an e-beam evaporator at a rate of 0.2 Å/s as a top electrode (TE) (60 μm × 60 μm) with a metal shadow mask. The bass pressure of the evaporator chamber was 4.7×10^{-7} Torr.

The structural characteristics and phase were confirmed using grazing incidence X-ray diffraction (GIXRD) (X'pert Pro) with Cu Kα radiation at a wavelength of 1.54 Å and a small incident angle (0.3°). The densification of the films was confirmed by X-ray reflectometry (XRR). A scanning probe microscope (SPM) (Park NX20, tapping mode) was employed to observe the surface morphology. X-ray photoelectron spectroscopy (XPS: Quantera SXM) was conducted to investigate the chemical compositions. The electrical characteristics of the devices were measured in air using an Agilent 4155 semiconductor parameter analyzer at room temperature.

3. Results and Discussion

The GIXRD spectra of the sol–gel-processed ZrO_2 layers were interpreted using the JCPDS database (811550). Figure 1a shows the GIXRD spectra from different annealing conditions: air, vacuum, and N_2. The peaks of all three devices matched well with the ZrO_2 peaks, implying that these devices have a ZrO_2 polycrystalline cubic structure. The diffraction peaks at 31.16°, 34.96°, 50.27°, and 59.74° correspond to the (111), (200), (220), and (311) crystal planes. The intensity of (111) in the XRD diffraction patterns of ZrO_2 films was favored, regardless of the annealing environment. The full width at half-maximum (FWHM) of a GIXRD peak is known to be closely related to the crystallite size. The crystalline size was calculated using the Scherrer equation, $D = k\lambda/\beta\cos(\theta)$, where λ is the X-ray wavelength (nm), θ is the Bragg angle, β is the width of the line at the half-maximum intensity, and k is a geometric factor (= 0.9). According to the Scherrer equation, the estimated crystalline sizes were 10.6, 12.7, and 4.2 nm for the (111) phase of ZrO_2 films annealing in air, a vacuum, and N_2, respectively. The ZrO_2 film annealed in a vacuum exhibited the greatest size, and the N_2-annealed film demonstrated a relatively small crystalline size [15]. Figure 1b presents the XRR curves of the annealed ZrO_2 corresponding to different annealing ambiences. It can be seen that the critical angles were 0.31° (in air), 0.32° (in a vacuum), and 0.31° (in N_2). Based on Buydens' method, the densities of the ZrO_2 films were calculated as 5.08, 5.39, and 5.02 g/cm^3. The obtained thicknesses of the ZrO_2 were 52.6, 53.1, and 61.5 nm [16].

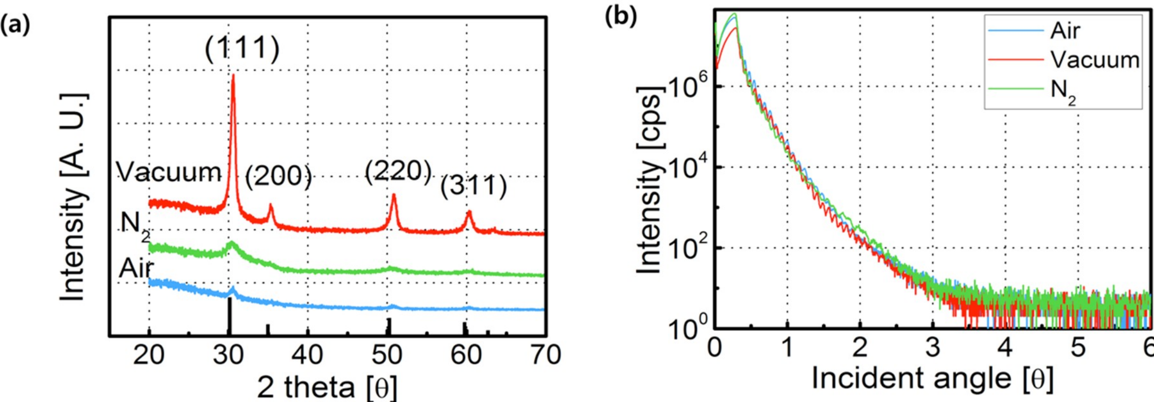

Figure 1. (**a**) XRD results of sol–gel-processed ZrO_2 films and (**b**) XRR results of ZrO_2 films annealed in air, vacuum, and N_2.

The SPM images of the sintered ZrO_2 layers (Figure 2) were used to confirm the surface morphology of each annealing ambience. The obtained root mean square (RMS) roughness values were 0.281, 0.444, and 0.198 nm.

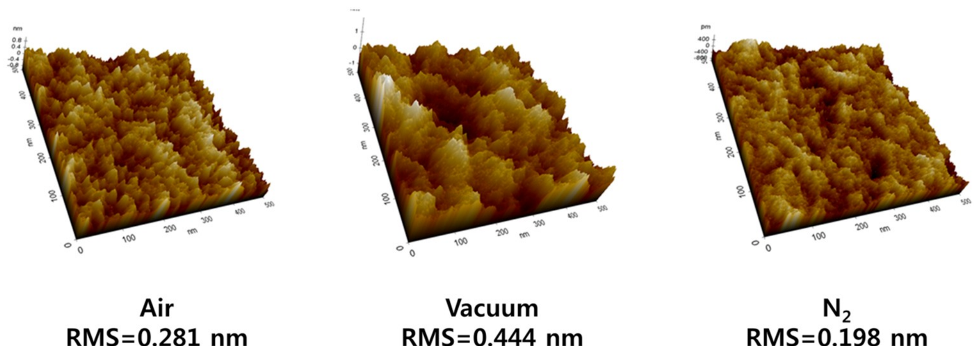

Figure 2. SPM images of ZrO_2 thin films annealed in air, vacuum, and N_2.

The chemical composition of ZrO_2 films annealed under different environment conditions was determined by XPS, where the O compositions were evaluated by assessing the O 1_s spectra in Figure 3a–c. The O 1s peak consists of three peaks, which occur at 530.0, 531.4, and 532.2 eV. The peak at 530.0 eV represents the oxygen ions (O^{2-}) ($O_{Lattice}$) combined with metal cations in ZrO_2. The peak at 531.4 eV represents the oxygen vacancy ($O_{Vacancy}$) in the structure. The peak at 532.2 eV represents the hydroxyl groups (-OH). Figure 3d shows the relative contents of the $O_{Lattice}$, $O_{Vacancy}$, and –OH of ZrO_2 films annealed in air, a vacuum, and N_2, respectively. The ZrO_2 films annealed in vacuum showed a relatively small quantity of oxygen vacancies.

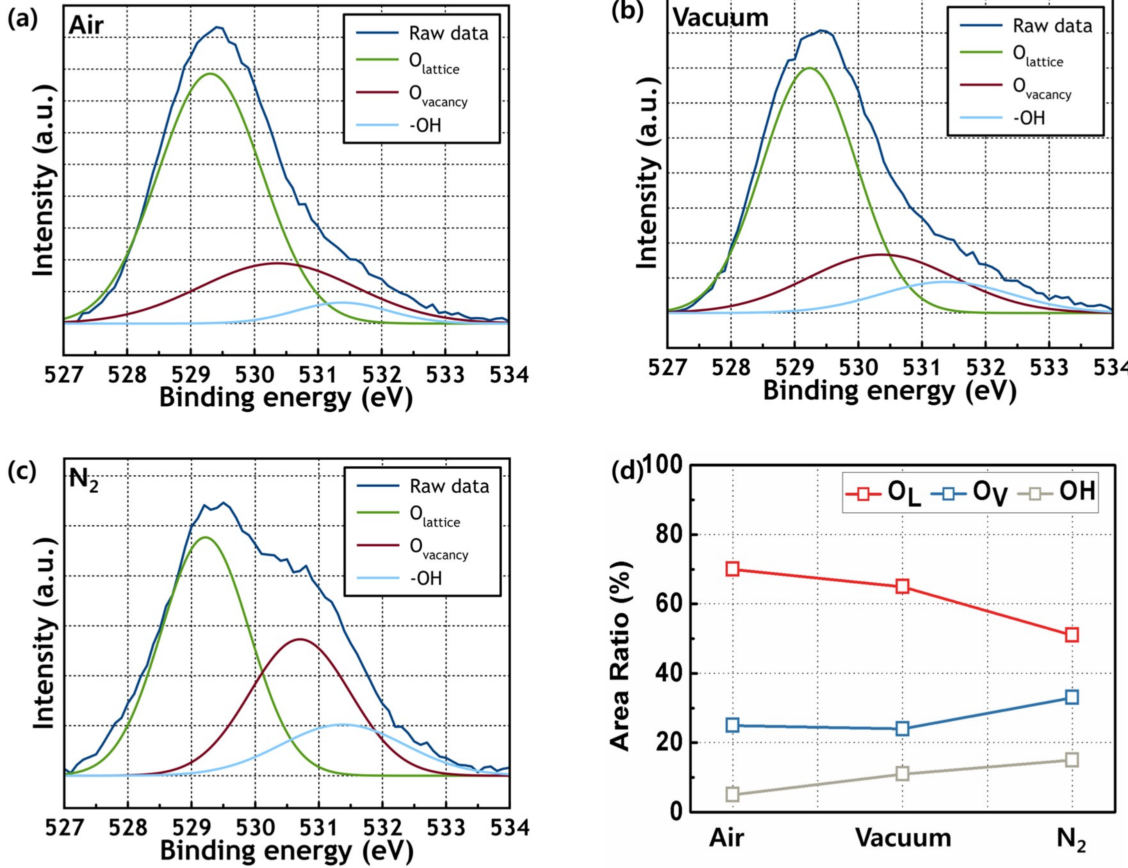

Figure 3. O 1s XPS spectra of ZrO_2 films annealed in (**a**) air, (**b**) vacuum, and (**c**) N_2. And (**d**) proportions of oxygen lattice, vacancy, and hydroxyl groups of fabricated films.

The I–V curves of the three samples (with a current compliance (CC) of 1 A) are shown in Figure 4a,b. The fabricated devices demonstrated a bipolar-mode RRAM switching property. It is well known that Ag/ZrO_2/ITO RRAM is the representative electrochemical metallization RRAM (ECM RRAM). Ag cations are much more diffusive than oxygen vacancies. During a SET process with a positive voltage bias on the top electrodes (TE), the ionized Ag cations penetrated through the ZrO_2 insulator layer to the bottom electrodes (ITO), forming a conductive bridge and thus moving to an LRS. Reversely, during a RESET process with a negative voltage bias on TE, the Ag cations moved back to TE. The conductive bridge no longer connected the bottom electrodes and the current decreased abruptly, creating a HRS [8,9].

Compared with the air and N_2-annealed device, the vacuum-annealed device exhibited a lower off-current in the HRS. The HRS/LRS values of the air and N_2-annealed devices were ~10^2, and those of the vacuum-annealed devices were ~10^3. As a result, the HRS/LRS ratio was 33 times greater than the RRAM, which consisted of ZrO_2 layers annealed in air and N_2. In particular, we could increase the HRS by approximately 10 times due to the decreased current leakage. The annealing process in a vacuum permitted the formation of denser films and high oxidation states with a small number of oxygen vacancies in ZrO_2 films with a low leakage current [17]. Figure 4c,d shows the distribution of the representative parameters, such as the HRS, LRS, SET voltage, and RESET voltages. In particular, the N_2-annealed ZrO_2 RRAM exhibited a relatively smooth SET and RESET. Multilevel storage capability can be successfully obtained [7,18]. More investigation is needed.

As already mentioned, during the LRS, the current flowed through a metallic bridge, known as the conductive filament. The current flowed through a finite resistance layer. This is in accordance with

the Ohmic current mechanism. Figure 5a presents the I–V curves in the LRS. The fabricated devices followed the linearity of the Ohmic current mechanism:

$$J = qn_0\mu V/d \tag{1}$$

where q is the electric charge, n_0 is the carrier density, μ is the carrier mobility, and d is the thickness of the resistive switching layer.

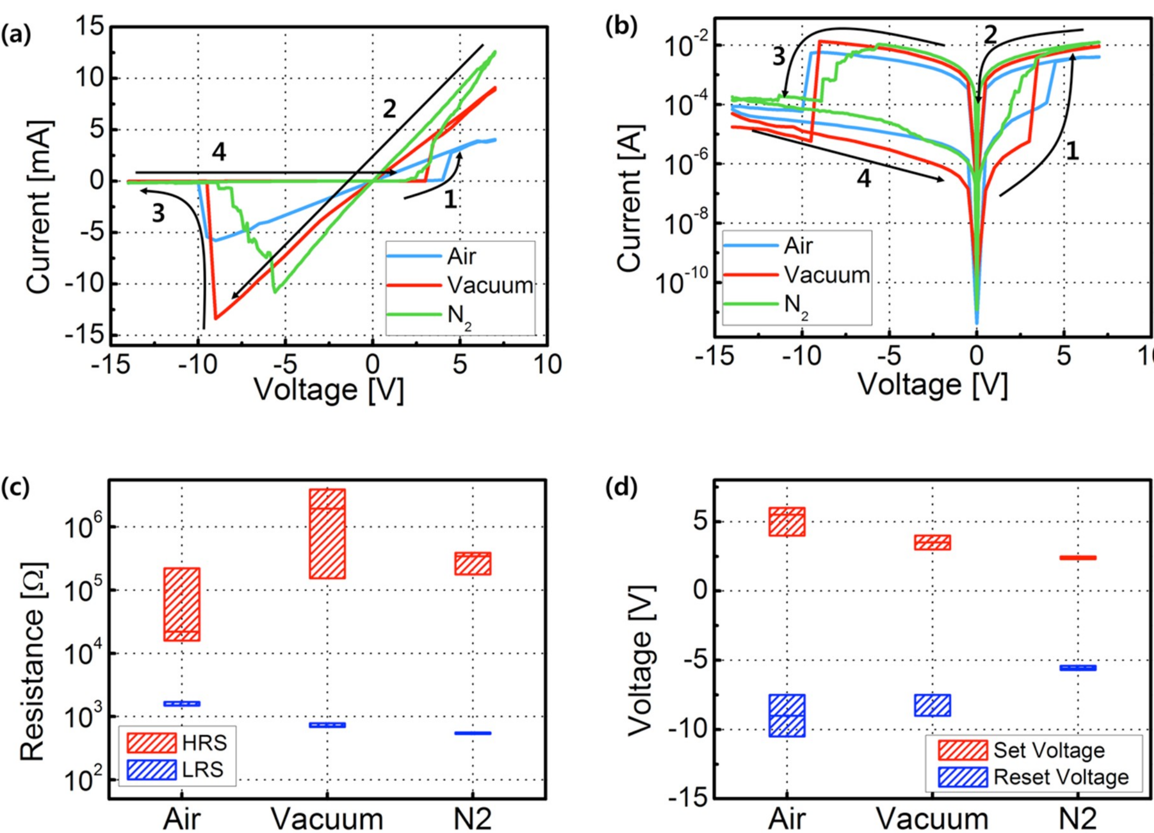

Figure 4. Representative I–V curves obtained from ITO/ZrO_2/Ag RRAM devices. The arrows and numbers indicate the voltage sweep directions. (**a**) Linear scale and (**b**) log scale, while (**c**) HRS/LRS values and (**d**) SET/RESET voltages.

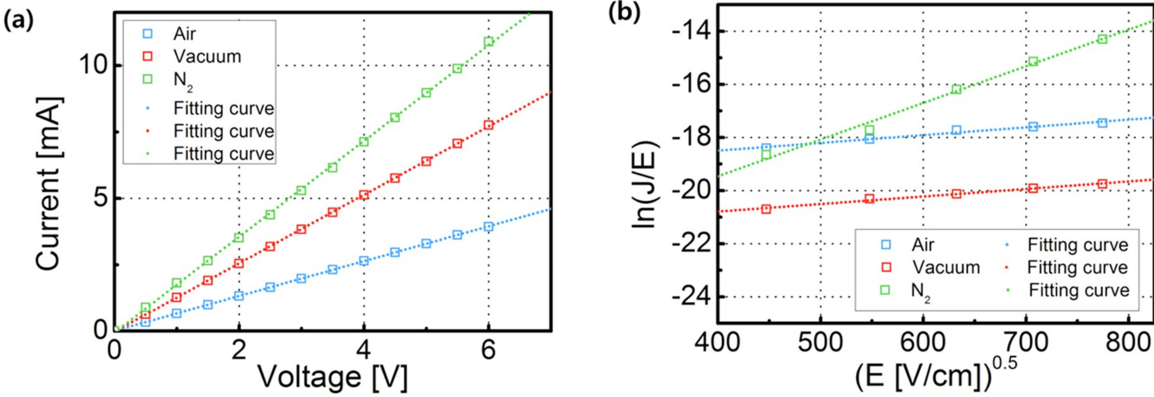

Figure 5. (**a**) Ohmic transport mechanism of LRS and (**b**) Poole–Frenkel transport mechanism of HRS of the fabricated RRAM devices, consisting of ZrO_2 films annealed in air, vacuum, and N_2.

In a HRS, Poole–Frenkel transport was the main mechanism. The defects or oxygen vacancies in the ZrO_2 layer acted as traps. When trapped electrons were thermally excited, they were able to move over the traps' potential, and the current could thus flow even though the filament was disconnected. This was confirmed by the linear fitting of the ln(J/E) vs. $E^{0.5}$ curve:

$$J = [q\mu N_C E] \exp\{-q\left[\varnothing_T - \left(\frac{qE}{\pi\varepsilon_0\varepsilon_d}\right)^{0.5}\right]/kT\}, \quad (2)$$

where q is the electric charge, μ is the electronic drift mobility, N_C is the density of states in the conduction band, E is the applied electric field, $\emptyset_T$ is the depth of the trap potential well, and ε_d is the dielectric constant for ZrO_2 [19].

The endurance and retention properties of the fabricated RRAM devices were then measured. The tested RRAM devices consisted of a 500 °C annealed ZrO_2 active layer in a vacuum, demonstrating a high HRS/LRS ratio. The resistance values of the HRS and LRS were obtained at +0.2 V, following programming (+7.0 V) and erasing (−14.0 V) for 50 ms. The measured resistance values of the HRS and LRS were found to last for 10^4 s without any significant deterioration, and for up to 100 continuous program/erase cycles with a resistive window of ~10^3, as shown in Figure 6. The fabricated Ag/ZrO_2/ITO devices exhibited a larger HRS/LRS ratio [20] and improved retention characteristics compared with other RRAM devices consisting of ZrO_2 layers [21]. In our case, the metal crystallization process is a critical rule to form the conductive filament. Thus, high-quality dielectric layers and interface are required to improve HRS/LRS, and non-volatile memory properties such as endurance and retention properties. The vacuum-annealed ZrO_2 films exhibited larger crystallinity and grain size, and denser film, and showed a relatively small quantity of oxygen vacancies. The vacuum annealing process helped to meet these requirements.

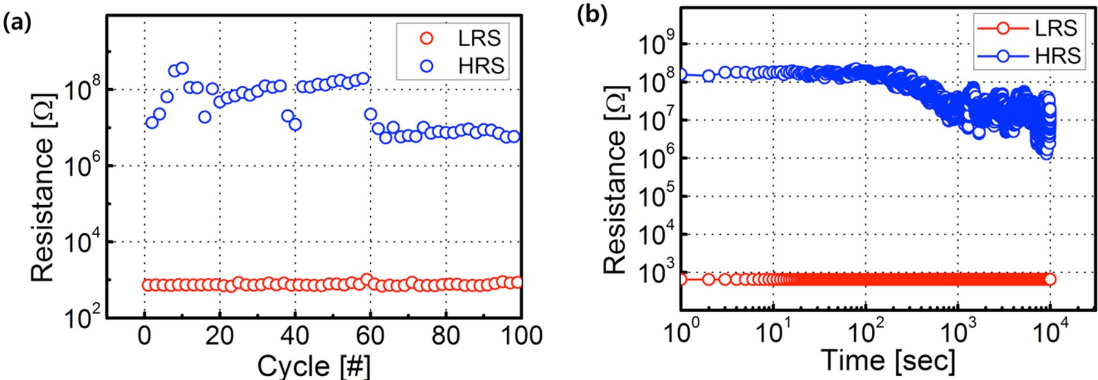

Figure 6. (**a**) Representative endurance properties and (**b**) retention properties of RRAM devices consisting of ZrO_2 films annealed in vacuum.

4. Conclusions

We investigated the annealing environment effect on ZrO_2-based RRAM devices. The fabricated devices exhibited conventional bipolar-switching memory properties. In particular, the vacuum-annealed ZrO_2 films exhibited larger crystallinity and grain size and denser film and showed a relatively small quantity of oxygen vacancies compared with the films annealed in air and N_2. These led to a decrease in the leakage current and an increase in the resistance ratio of the HRS/ LRS and successfully improved the non-volatile memory properties, such as endurance and retention characteristics. The HRS and LRS values were found to last for 10^4 s without any significant degradation.

Author Contributions: Conceptualization, J.J.; Experiments and Data Analysis, S.H., H.L., W.-Y.L. and B.J.; Investigation, H.-J.K., K.K. and J.J.; Writing—Original Draft Preparation, S.H. and H.L.; Writing—Review and Editing, J.J., K.K. and H.-J.K.

Funding: This research was supported by the Basic Science Research Program through the National Research Foundation of Korea (NRF) funded by the Ministry of Education (NRF-2016R1D1A3B03930896) and the National Research Foundation of Korea (NRF) grant funded by the Korea government (MSIT) (2019R1F1A1059788).

Conflicts of Interest: The authors declare no conflicts of interest.

References

1. Li, Y.; Long, S.; Zhang, M.; Liu, Q.; Shao, L.; Zhang, S.; Wang, Y.; Zuo, Q.; Liu, S.; Liu, M. Resistive switching properties of Au/ZrO_2/Ag structure for low-voltage nonvolatile memory applications. *IEEE Electron Device Lett.* **2010**, *31*, 117–119.
2. Puglisi, F.M.; Larcher, L.; Bersuker, G.; Padovani, A.; Pavan, P. An empirical model for RRAM resistance in low- and high-resistance states. *IEEE Electron Device Lett.* **2013**, *34*, 387–389. [CrossRef]
3. Chang, K.C.; Tsai, T.M.; Chang, T.C.; Wu, H.H.; Chen, J.H.; Syu, Y.E.; Chang, G.W.; Chu, T.J.; Liu, G.R.; Su, Y.T.; et al. Characteristics and mechanisms of silicon-oxide-based resistance random access memory. *IEEE Electron Device Lett.* **2013**, *34*, 399–401. [CrossRef]
4. Song, S.; Cho, B.; Kim, T.W.; Ji, Y.; Jo, M.; Wang, G.; Choe, M.; Kahng, Y.H.; Hwang, H.; Lee, T. Three-dimensional integration of organic resistive memory devices. *Adv. Mater.* **2010**, *22*, 5048–5052. [CrossRef] [PubMed]
5. Zhuge, F.; Peng, S.; He, C.; Zhu, X.; Chen, X.; Liu, Y.; Li, R.W. Improvement of resistive switching in Cu/ZnO/Pt sandwiches by weakening the randomicity of the formation/rupture of Cu filaments. *Nanotechnology* **2011**, *22*, 275204. [CrossRef] [PubMed]
6. Jang, J.; Pan, F.; Braam, K.; Subramanian, V. Resistance switching characteristics of solid electrolyte chalcogenide Ag_2Se nanoparticles for flexible nonvolatile memory applications. *Adv. Mater.* **2012**, *24*, 3573–3576. [CrossRef]
7. Jang, J. Effect of electrode material on characteristics of non-volatile resistive memory consisting of Ag_2S nanoparticles. *AIP Adv.* **2016**, *6*, 075006. [CrossRef]
8. Jang, J.; Subramanian, V. Effect of electrode material on resistive switching memory behavior of solution-processed resistive switches: Realization of robust multi-level cells. *Thin Solid Films.* **2017**, *625*, 87–92. [CrossRef]
9. Lee, S.; Kim, T.; Jang, B.; Lee, W.Y.; Song, K.C.; Kim, H.S.; Do, S.Y.; Hwang, S.B.; Chung, S.; Jang, J. Impact of Device Area and Film Thickness on Performance of Sol-gel Processed ZrO_2 RRAM. *IEEE Electron Device Lett.* **2018**, *39*, 668–671. [CrossRef]
10. Jang, J.; Kitsomboonloha, R.; Swisher, S.L.; Park, E.S.; Kang, H.; Subramanian, V. Transparent high-performance thin film transistors from solution processed SnO_2/ZrO_2 gel-like precursors. *Adv. Mater.* **2013**, *25*, 1042–1047. [CrossRef] [PubMed]
11. Jang, J.; Kang, H.; Chakravarthula, H.C.N.; Subramanian, V. Fully inkjet-printed transparent oxide thin film transistors using a fugitive wettability switch. *Adv. Electron. Mater.* **2015**, *1*, 1500086. [CrossRef]
12. Kwon, H.J.; Jang, J.; Grigoropoulos, C.P. Laser Direct Writing Process for Making Electrodes and High-k Sol–Gel ZrO_2 for Boosting Performances of MoS_2 Transistors. *ACS Appl. Mater. Interfaces* **2016**, *8*, 9314–9318. [CrossRef] [PubMed]
13. Chen, P.Y.; Yu, S. Impact of vertical RRAM device characteristics on 3D cross-point array design. In Proceedings of the 2014 IEEE 6th International Memory Workshop (IMW), Taipei, Taiwan, 18–21 May 2014.
14. Zackriya, V.M.; Kittur, H.M.; Chin, A. A novel read scheme for large size on resistor resistive random access memory array. *Sci. Rep.* **2017**, *7*, 42375. [CrossRef] [PubMed]
15. Khan, W.; Khan, F.; Ajmal, H.M.S.; Huda, N.U.; Kim, S.D. Evolution of structural and optical properties on ZrO_2 nanorods grown on vacuum annealed seed crystallites. *Nanomaterials* **2018**, *8*, 68. [CrossRef] [PubMed]
16. Dane, A.D.; Veldhuis, A.; de Boer, D.K.G.; Leenaers, A.J.G.; Buydens, L.M.C. Application of genetic algorithms for characterization of thin layered materials by glancing incidence X-ray reflectometry. *Physica B* **1998**, *253*, 254–268. [CrossRef]

17. Cai, W.; Chu, Z.; Wei, J.; Fang, Z.; Ning, H.; Zheng, Z.; Zhou, S.; Yao, R.; Peng, J.; Lu, X. A simple method for high performance solution processed, amorphous ZrO_2 gate insulator TFT with a high concentration precursors. *Materials* **2017**, *10*, 972. [CrossRef] [PubMed]
18. Wei, X.; Hung, H.; Ye, C.; Wei, W.; Zhou, H.; Chen, Y.; Zhang, R.; Zhang, L.; Xia, Q. Exploring the role of nitrogen incorporation in ZrO_2 resistive switching film for enhancing the device performance. *J. Alloy. Compd.* **2019**, *755*, 1301–1306. [CrossRef]
19. Sze, S.M. Current transport and maximum dielectric strength of silicon nitride films. *J. Appl. Phys.* **1967**, *38*, 2951–2956. [CrossRef]
20. Huang, R.; Yan, X.; Ye, S.; Kashtiban, R.; Beanland, R.; Morgan, K.A.; Charlton, M.D.B.; de Groot, C.H. Compliance-free $ZrO_2/ZrO_{2-x}/ZrO_2$ resistive memory with controllable interfacial multistate switching behavior. *Nanosc. Res. Lett.* **2017**, *12*, 384. [CrossRef] [PubMed]
21. Parreira, P.; Paterson, G.W.; McVitie, S.; MacLaren, D.A. Stability, bistability and instability of amorphous ZrO_2 resistive memory devices. *J. Phys. D Appl. Phys.* **2016**, *49*, 095111. [CrossRef]

© 2019 by the authors. Licensee MDPI, Basel, Switzerland. This article is an open access article distributed under the terms and conditions of the Creative Commons Attribution (CC BY) license (http://creativecommons.org/licenses/by/4.0/).